Palaeogeography, Palaeoclimatology, Palaeoecology 612 (2023) 111380

Contents lists available at ScienceDirect

Palaeogeography, Palaeoclimatology, Palaeoecology

journal homepage: www.elsevier.com/locate/palaeo

Centennial-scale variability of the Indian Summer Monsoon during the middle to late Holocene and its links with ENSO activity

Huanyu Sun [a], Xingqi Liu [a,*], Xin Mao [b], Weihan Jia [c,d], Ulrike Herzschuh [c,d,e]

[a] College of Resource Environment and Tourism, Capital Normal University, Beijing 100048, China
[b] Institute of Hydrogeology and Environmental Geology, Chinese Academy of Geological Sciences, Shijiazhuang 050061, China
[c] Polar Terrestrial Environmental Systems Research Group, Alfred Wegener Institute Helmholtz Centre for Polar and Marine Research, Potsdam 14473, Germany
[d] Institute of Environmental Science and Geography, University of Potsdam, Potsdam 14476, Germany
[e] Institute of Biochemistry and Biology, University of Potsdam, Potsdam 14476, Germany

ARTICLE INFO

Editor: P. Hesse

Keywords:
Holocene
Indian Summer Monsoon
ENSO
Centennial-scale

ABSTRACT

Relatively little is known about the relationship between the Indian summer monsoon (ISM) and the El Niño-Southern Oscillation (ENSO) on the centennial timescale during the Holocene. We present a well-dated high-resolution X-ray fluorescence (XRF) scanning record from a sediment core from Lake Qionghai on the south-eastern Tibetan Plateau, which reveals the impact of ENSO activity on ISM variability. The results indicate a gradual drying of the regional climate on the sub-orbital timescale, which is in broad agreement with ISM changes controlled by Northern Hemisphere summer insolation. Additionally, centennial-scale drought events occurred at around 6230–5740, 4620–4250, 3820–3540, 3210–2440, 2180–1320, and 1000–615 cal yr B.P. and are consistent with enhanced ENSO activity, documenting the occurrence of ENSO-related drought events in the Holocene. Both ISM oscillations and ENSO variability show significant 350-yr, 500-yr, and 800-yr cyclicities, and there is a highly significant negative relationship between the ISM and ENSO at these cyclicities, indicating that a weak ISM was related to increased ENSO intensity, and vice versa. Our findings provide evidence for the modulation of ISM intensity by ENSO variability on the centennial timescale during the Holocene.

1. Introduction

As a major global climate system the Indian Summer Monsoon (ISM) is the primary moisture source for many sub-tropical Asian regions (Overpeck et al., 1996). There are numerous views on the driving mechanisms of the ISM on different timescales. On the orbital timescale, insolation and ice volume play the dominant roles in controlling ISM variability (Cai et al., 2015; Fleitmann et al., 2007; Kathayat et al., 2016; Kutzbach et al., 2008; Liu et al., 2020; Yuan et al., 2004). On the millennial timescale, changes in latent heat influxes from the southern Indian Ocean (Clemens and Prell, 2003; Leuschner and Sirocko, 2003), ice-rafted detritus (IRD) in North Atlantic deep-sea sediments (Hong et al., 2005; Gupta et al., 2003, 2005), and Indian Ocean sea-surface temperatures (SSTs) (Zhang et al., 2017) can be explained by changes in the ISM. On the centennial timescale, solar activity is often invoked to explain changes in the ISM (Li et al., 2015), but other drivers have also been considered such as tropical ocean-atmosphere coupling (Tiwari et al., 2015), the Indian Ocean Dipole (Li et al., 2017), and North Atlantic sea-surface temperatures (Sun et al., 2020).

The El Niño-Southern Oscillation (ENSO) is a coupled ocean-atmosphere phenomenon originating in the tropical Pacific. It plays an important role not only in precipitation over the Asian and African areas but also in global climate changes (Cane, 2005; Deser et al., 2010; Hong et al., 2005; McPhaden et al., 2006). El Niño/La Niña shifts the location of the tropical Walker circulation and effects a rainfall deficit/excess by suppressing/enhancing the convection over the Indian region (Fischer et al., 2005; Kumar et al., 1999; Reason et al., 2000). On interannual to decadal timescales, the relationship between ENSO and the ISM is well known to be anti-correlated during the last 200 years (Kumar et al., 2006; Shukla and Paolino, 1983; Tan et al., 2016; Torrence and Webster, 1999; Wang et al., 2008; Webster et al., 1998). On the centennial timescale, studies have focused mainly on high-resolution climate records covering the past 1000–2000 yr. These studies document significant dry climate episodes in the ISM region during the Current Warm Period (CWP) and the Medieval Warm Period (MWP), resembling enhanced El Niño-like conditions (Gu et al., 2020; Tan et al., 2019;

* Corresponding author.
E-mail address: xqliu@niglas.ac.cn (X. Liu).

https://doi.org/10.1016/j.palaeo.2022.111380
Received 12 July 2022; Received in revised form 22 December 2022; Accepted 29 December 2022
Available online 4 January 2023

Tejavath et al., 2019). On the sub-millennial timescale, variations in ISM moisture variability during the middle and late Holocene were negatively correlated with warm ENSO events, and ENSO acts as an internal forcing mechanism for amplifying the low-amplitude fluctuations in external solar irradiation (Ming et al., 2020; Sun et al., 2017). On the sub-orbital timescale, with the increasing frequency of ENSO episodes during the mid-Holocene, ENSO may have played the dominant role in driving the ISM and associated regional hydrological changes, and the weakening of the ISM after 5 ka was attributed to ENSO amplification (Band et al., 2018; Hillman et al., 2017; Srivastava et al., 2017). However, it is unclear whether ENSO had an influence on the ISM on the centennial timescale during the Holocene, and their possible phase relationship is also unclear. Therefore, it is necessary to provide continuous and high-resolution records to improve our understanding of the effects of ENSO variability on Holocene climate changes in the Indian monsoon region.

With reference to the modern summer monsoon system, Lake Qionghai, located on the southeastern margin of the Tibetan Plateau, is a typical region influenced by the ISM (Fig. 1). We obtained a well-dated high-resolution record of element contents based on X-ray fluorescence (XRF) scanning of a sediment core from Lake Qionghai. Our specific objectives were to reconstruct the history of the ISM during the middle

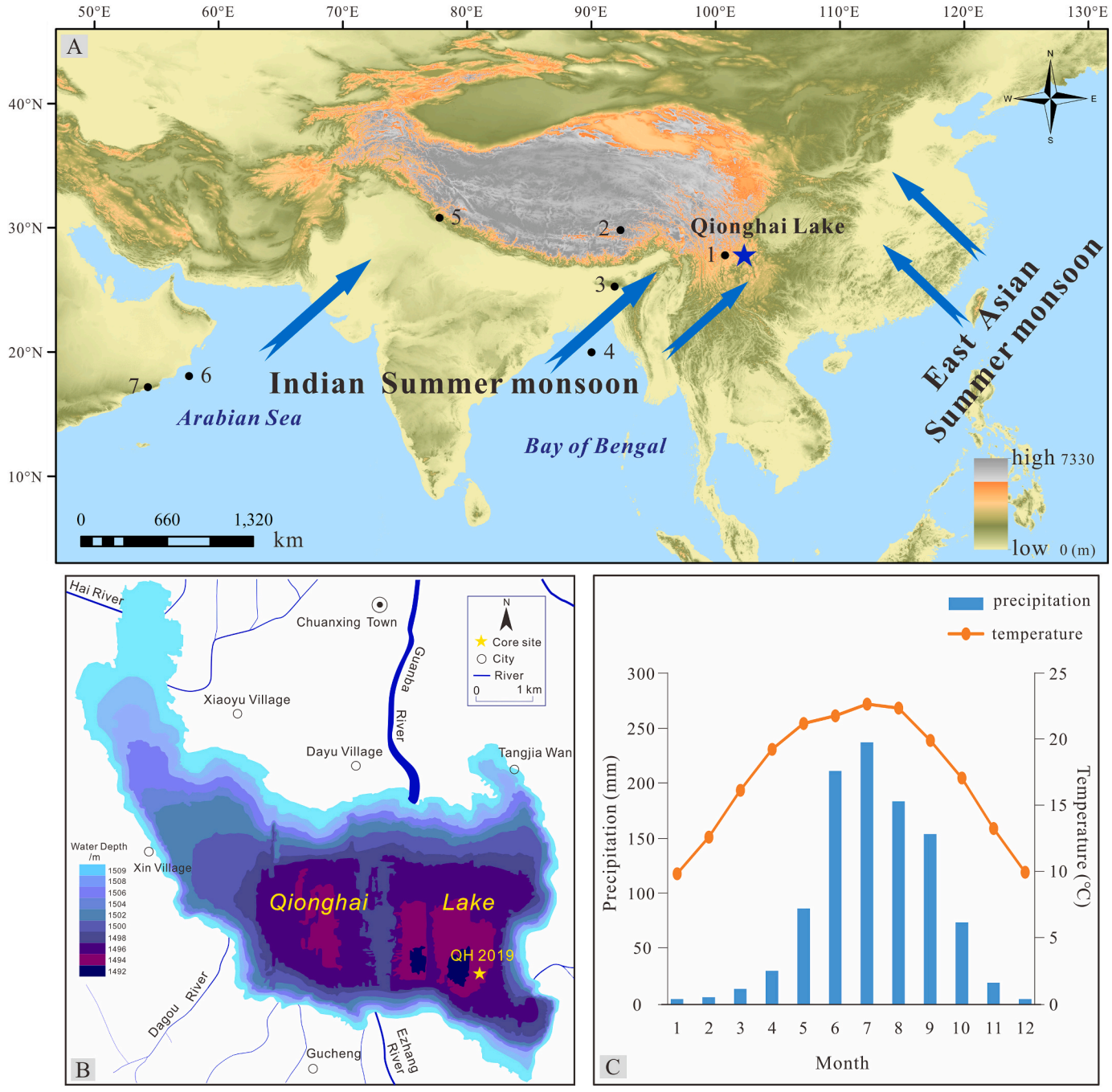

Fig. 1. A) Location of Lake Qionghai (star) and the paleoclimate records mentioned in the text: (1) Lake Lugu (Zhang et al., 2018), (2) Paru Co (Bird et al., 2014), (3) Mawmluh Cave (Berkelhammer et al., 2012), (4) core SO188-342KL from the Bay of Bengal (Contreras-Rosales et al., 2014), (5) Bittoo Cave (Kathayat et al., 2016), (6) Hole ODP723A in the Arabian Sea (Gupta et al., 2003), (7) Qunf Cave (Fleitmann et al., 2003). B) bathymetry of Lake Qionghai and the core site (star). C) Monthly climate data from Xichang meteorological station, showing the average monthly precipitation and temperature from 1981 CE to 2010.

and late Holocene, and to explore its possible links with ENSO activity on the centennial timescale.

2. Study site

Lake Qionghai (27°47′34″–27°51′57″N and 102°16′3″–102°20′43″E, 1510 m a.s.l.), is an open lake on the southeastern edge of the Tibetan Plateau (Fig. 1A). The lake has an area of 31 km^2, a maximum water depth of 34 m, and an average water depth of 14 m. The catchment area covers 310 km^2, and the altitude ranges between 1507 and 3263 m. Hydrologically the lake is fed mainly by the Guanba River and the Ezhang River, which enter the lake from the east side, and it is drained via the Hai River on the north-western side (Fig. 1B).

The study region has a typical subtropical monsoon climate, which is mainly influenced by the ISM. Based on records from the nearest meteorological station at Xichang (27°54′N, 102°16′E, 1591 m a.s.l.), between 1981 and 2010, the mean annual precipitation and mean annual temperature were 1024 mm and 17.2 °C, respectively (Fig. 1C). Statistical data also show that ~92% of the annual precipitation falls between May and October. The warmest month is July, with a mean monthly temperature of 22.6 °C, and the coldest month is January, with a mean monthly temperature 9.9 °C. The vegetation is subtropical evergreen broadleaved forest and evergreen and deciduous broadleaved mixed forest (Chen et al., 2015).

3. Materials and methods

In 2019, an 18.05-m-long sediment core (QH2019) was extracted from the depocenter of Lake Qionghai at a water depth of 18 m (27°48′25.56″N, 102°19′52.47″E; 1510 m a.s.l.) (Fig. 1B), using the UWITEC drilling platform. The sediment core was split along its central axis with a core-cutting machine in our laboratory. The half cores were photographed, and the lithology was described. One half-core was scanned using an ITRAX X-ray Fluorescence (XRF) Core Scanner (Cox Analytical System) (Croudace et al., 2006). Finally, samples were taken at 1-cm intervals and magnetic susceptibility was measured at 2-cm intervals. All the sampling and experiments were performed in the College of Resource Environment and Tourism, Capital Normal University.

The fresh core surface was carefully smoothed before XRF scanning and covered with Ultralene film to prevent desiccation during scanning. The scanner was equipped with a Rh X-ray tube as an energy source for obtaining optical and X-ray images, which was conducted while measuring the element contents. Operating conditions were: voltage 30 kV, current 55 mA, step size 1-mm, exposure time 5 s. Element variations are expressed as counts per second (CPS). We screened elements with CPS > 200 as the standard to ensure data quality. Elements with low raw counts were excluded as they were close to the detection limits of the ITRAX and may even be measurement noise. To avoid the matrix effect, a centered log-ratio (CLR) transformation was applied to calibrate the element data (Weltje et al., 2015). The element scanning results were analyzed using principal component analysis (PCA) to summarize the variance with a reduced number of variables. The PCA was implemented using CANOCO v. 5 (ter Braak and Smilauer, 2012). Spectral analysis was conducted using PAST with the REDFIT and rectangular window options (Hammer et al., 2001), and band-pass filter analysis was conducted using ACYCLE v. 2.4 (Li et al., 2019).

Low-frequency (0.47 kHz) magnetic susceptibility (χ_{lf}) was measured using a Bartington MS2 susceptometer with an MS2B dual frequency sensor (Bartington Instruments, Ltd., Witney, UK), following standard procedures.

The core chronology is based on Accelerator Mass Spectrometry (AMS) ^{14}C dating conducted on 26 samples of plant residues, charcoal, and bulk organic sediments. The measurements were made by Beta Analytic Inc., Miami, USA (Table 1). The ^{14}C dates were converted to calendar ages using the IntCal20 calibration curve (Reimer et al., 2020).

Table 1
AMS dating results and calibrated ages of samples from sediment core QH2019 from Lake Qionghai.

Sample No.	Lab I.D.	Depth (cm)	Analyzed Material	$\delta^{13}C$ (‰)	AMS ^{14}C age (yr B.P.)	Calibrated age (cal yr B.P.)
QH-1-2 32	Beta-551,501	42	Organic sediment	−25.8	1720 ± 30	1702–1559
QH-1-2 86	Beta-551,502	96	Organic sediment	−24.1	2740 ± 30	2885–2765
QH-1-2 154	Beta-551,503	164	Organic sediment	−24.2	2620 ± 30	2780–2724
QH-1-3 90	Beta-551,504	232	Organic sediment	−25.1	2550 ± 30	2750–2692
QH-1-4 102	Beta-551,505	390	Organic sediment	−24.8	3110 ± 30	3386–3237
QH-1-5 58	Beta-551,506	482	Organic sediment	−25.4	2970 ± 30	3229–3025
QH-1-5 140	Beta-551,507	564	Plant material	−26.7	750 ± 30	728–664
QH-1-5 148	Beta-568,279	572	Charred material	−26.0	850 ± 30	798–690
QH-1-6 84	Beta-551,508	620	Organic sediment	−25.0	2120 ± 30	2155–1999
QH-2-6 59	Beta-571,255	762	Organic sediment	−25.6	1190 ± 30	1184–1052
QH-2-6 125	Beta-571,256	828	Organic sediment	−25.9	1590 ± 30	1544–1408
QH-2-7 91	Beta-571,257	897	Organic sediment	−27	1900 ± 30	1900–1770
QH-2-8 61	Beta-572,852	1002	Organic sediment	−27.7	2410 ± 30	2498–2350
QH-2-8 151	Beta-571,259	1092	Organic sediment	−28	2840 ± 30	3039–2865
QH-2-9 132	Beta-571,260	1207	Organic sediment	−28.3	3500 ± 30	3855–3692
QH-2-10 78	Beta-571,261	1287	Organic sediment	−28	4020 ± 30	4536–4420
QH-2-10 163	Beta-571,262	1372	Organic sediment	−27.7	4580 ± 30	5327–5272
QH-2-11 99	Beta-571,263	1442	Organic sediment	−28.2	4950 ± 30	5735–5605
QH-2-11 169	Beta-571,264	1512	Organic sediment	−28.9	5310 ± 30	6185–5995
QH-2-12 83	Beta-571,265	1562	Organic sediment	−28.9	5420 ± 30	6289–6185
QH-2-12 113	Beta-572,853	1592	Organic sediment	−27.9	5400 ± 30	6287–6177
QH-2-12 173	Beta-572,854	1652	Organic sediment	−27.8	5710 ± 30	6567–6410
QH-2-14′ 115	Beta-571,270	1728	Organic sediment	−28.2	5800 ± 30	6670–6503
QH-2-13 124	Beta-571,268	1732	Organic sediment	−28.4	6080 ± 30	7014–6853
QH-2-13 164	Beta-571,269	1772	Organic sediment	−28.4	6070 ± 30	7007–6846
QH-2-14′ 175	Beta-571,271	1788	Organic sediment	−28.6	6030 ± 30	6951–6789

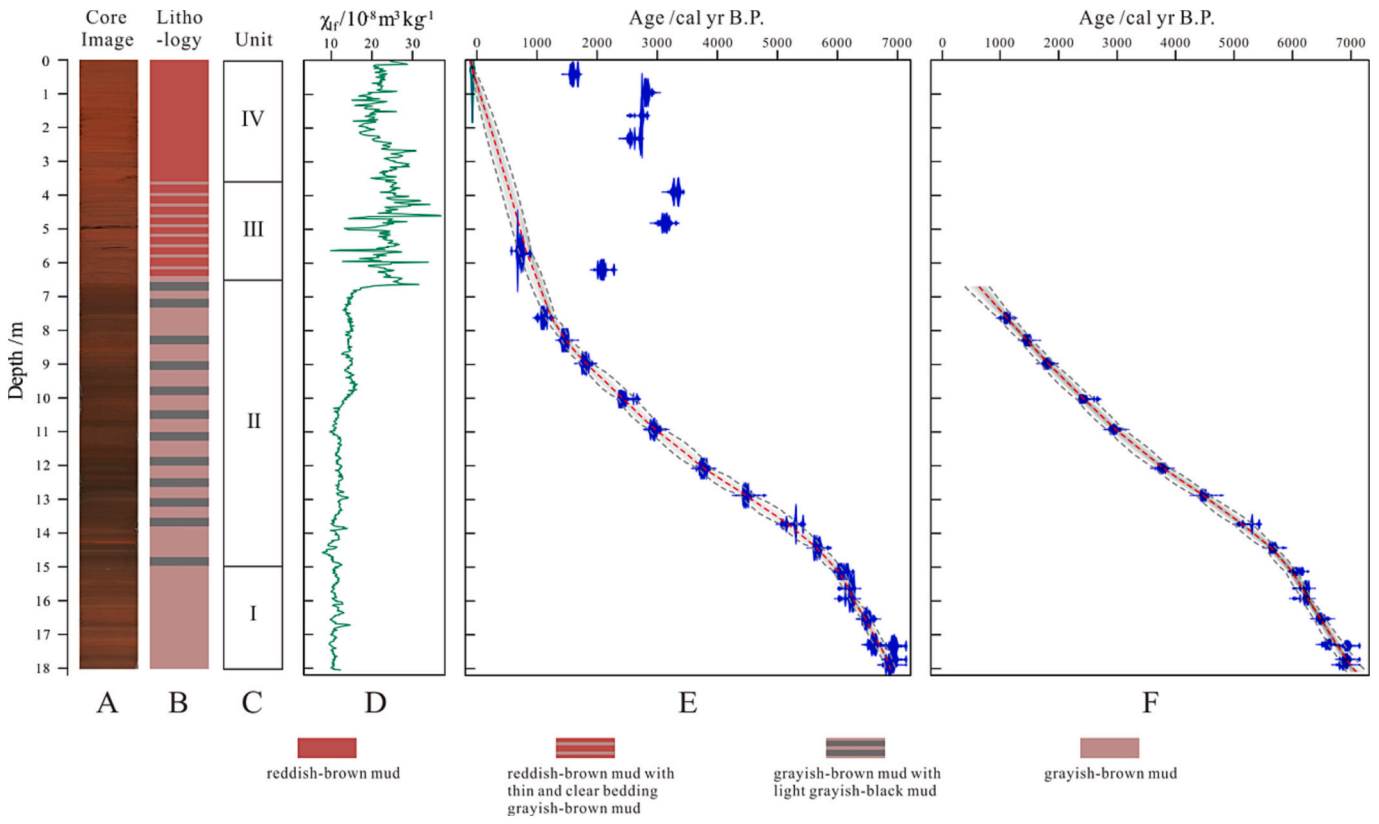

Fig. 2. (A) Core image, (B) sedimentary lithology, (C) lithologic units, (D) magnetic susceptibility profile for core QH2019, (E) Bacon age-depth model for the intervals of 18.05–0 m, and (F) 18.05–6.71 m. The grey dotted lines indicate the 95% confidence limits and the dashed red line shows the best fit ages based on the weighted mean age for each depth interval. (For interpretation of the references to colour in this figure legend, the reader is referred to the web version of this article.)

Undated intervals were interpolated using the Bacon program under the R platform (Fig. 2) (Blaauw and Christen, 2011).

4. Results

4.1. Lithology and chronology

The sediments of core QH2019 can be divided into four lithological units, from bottom to top: Unit I (18.05–15.00 m), grayish-brown mud; Unit II (15.00–6.50 m), alternating layers of grayish-brown and grayish-black mud; Unit III (6.50–3.56 m), reddish-brown mud partly intercalated with thin layers of grayish-brown mud with clear bedding; and Unit IV (3.56–0 m), reddish-brown mud (Fig. 2A, B, C).

There is a good relationship between depth and calendar age obtained from bulk organic sediments in the interval of 18.05–6.71 m, and the ages extrapolated to 5.72 m and 5.64 m depth are consistent with the ages based on plant residues and charcoal from these two depths (Fig. 2E). This indicates that there is no significant radiocarbon reservoir effect for ages based on bulk organic sediments. Considering that the magnetic susceptibility and the ^{14}C ages of the organic sediments above 6.71 m are clearly anomalous (Fig. 2D, E), we focus on the climatic and environmental changes between 18.05 m and 6.71 m. Based on the Bacon age-depth model, this depth interval spans ~6300 years from 7000 to 615 cal yr B.P. (Fig. 2F). The sedimentation rate has the range of 1.01–5.17 mm/yr and the average of 2.06 mm/yr. However, the sedimentation rate (with the average of 10 mm/yr over the depth interval of 6.71–0 m) is much higher than that over the interval of 18.05–6.71 m. This is possibly the result of anthropic activities in the drainage basin or other environmental perturbations. Natural disasters including earthquakes and landslides have occurred frequently in the Xichang area since the Ming and Qing Dynasties (Guo et al., 2014; Zhu, 2005). The forest cover was 80% during the Han Dynasty but substantial forest clearance occurred during the Ming and Qing Dynasties (Zhu, 2011). Deforestation would be expected to increase the rate of soil loss from the catchment and thus increase the sedimentation rate.

4.2. Element variations

The element profiles transformed by CLR for core QH2019 are shown in Fig. 3. The Ca profile shows a similar pattern to that of Sr; the profiles of Ti, Fe, Rb, K, Zr, and Si are similar; and the profile of Mn is different from that of the other elements. The PCA results show that the first two eigenvectors (PC1 and PC2) account for 86.2% of the total variance (Fig. 4 and Table 2). PC1 accounts for 70.1% of the total variance, and PC2 explains 16.2%. Ca and Sr have positive loadings on PC1 and Ti, Fe, Rb, Si, K, Zr have negative loadings. Mn has a high loading on PC2.

Minerogenic sediment input from the catchment is mainly reflected by Ti, K, Fe, Si and Rb, while autochthonous sediments are characterized by Ca and Sr (Kasper et al., 2015; Koinig et al., 2003; Kylander et al., 2011; Morellón et al., 2009). PC1 is characterized by the high positive loadings of Ca and Sr and high negative loadings for all the allochthonous elements. Therefore, PC1 is interpreted as reflecting the relative proportions of autochthonous carbonate precipitation and minerogenic input from the catchment. Positive sample scores on PC1 are taken to indicate increased carbonate precipitation during evaporative concentration of the lake water, accompanied by a lowering of the lake level (Marshall et al., 2011); whereas negative sample scores represent higher allochthonous clastic input caused by enhanced surface runoff resulting from increased precipitation (Kasper et al., 2012). Therefore, PC1 can be interpreted as an indicator of monsoon precipitation variations.

Ti, Fe, and Rb have the largest negative loadings on PC1 and thus they can be used to trace terrigenous sediment fluxes, and in the context

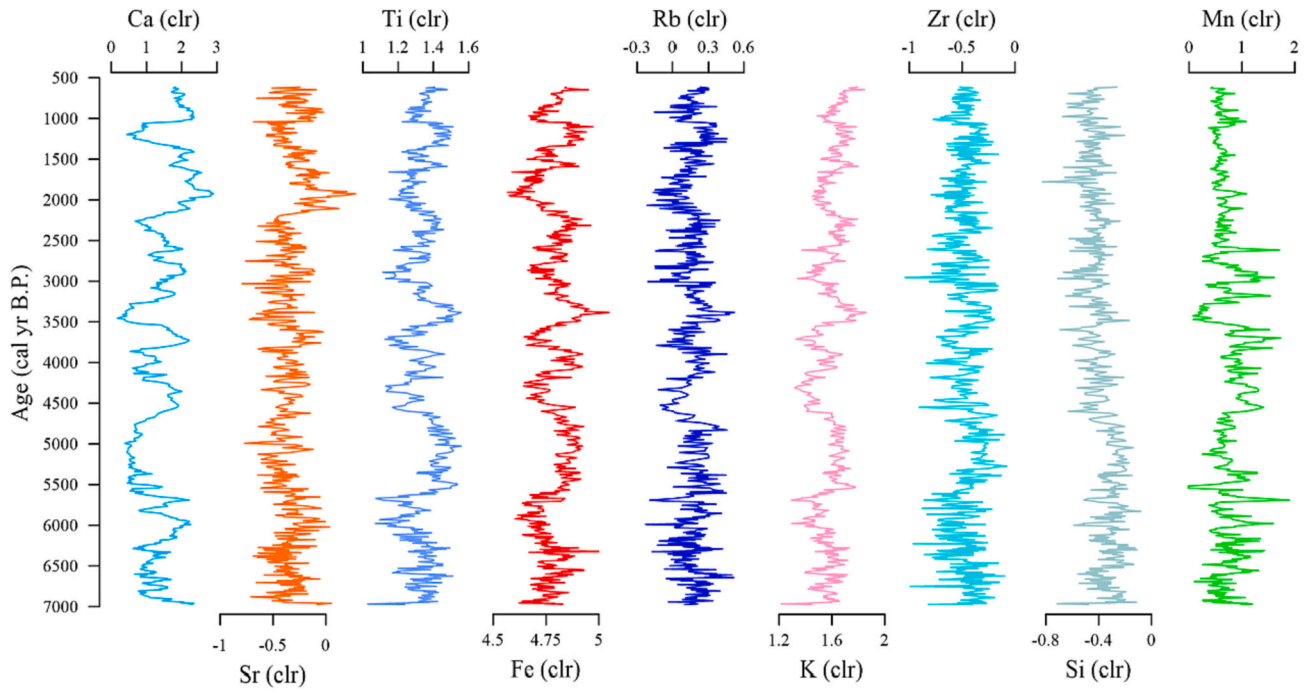

Fig. 3. Age profiles of representative elements for core QH2019.

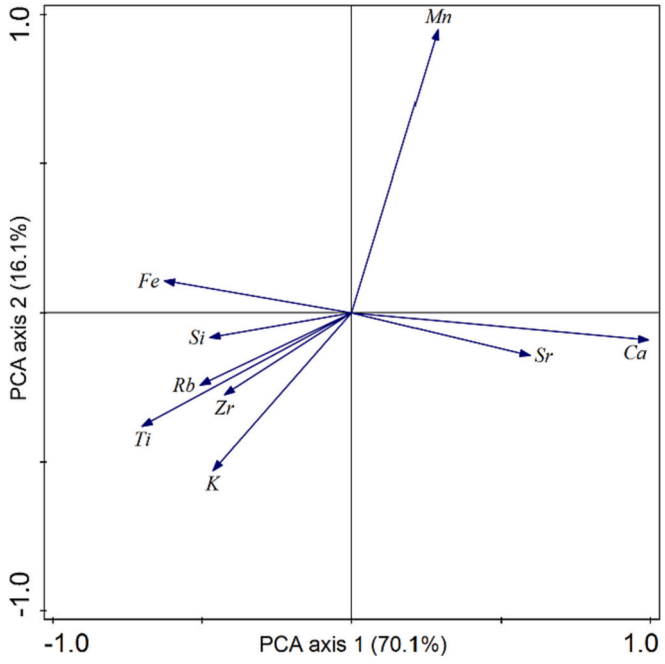

Fig. 4. PCA biplot of the variable loadings on PCA 1 and 2 for core QH2019.

of Lake Qionghai they can be regarded as proxies of rainfall and runoff (Arnaud et al., 2012; Haug et al., 2003; Haug et al., 2001). Ca and Sr have the largest positive loadings and are proxies of authigenic sediment production (Bajard et al., 2015). Therefore, the ratios of Ti/Ca, Fe/Ca, and Rb/Sr can be used to assess the material sources of the lake sediments and to distinguish the relative contribution of authigenic sediments and exogenous materials (Adegbie et al., 2003; Clift et al., 2014; Fernández et al., 2013; Stuut et al., 2014). High values of Ti/Ca, Fe/Ca, and Rb/Sr are generally associated with intensified clastic inputs, indicating enhanced monsoon and increased precipitation, and vice versa.

Table 2
PCA results. (A) Eigenvalues for the 9 obtained components. The percentage of the variance explained by each axis is shown. (B) Factor loading for each variable on PC1 and PC2.

(A)	Eigenvalue	Cumulative explained variance
Axis 1	0.7012	70.12
Axis 2	0.1607	86.19
(B)	Resp.1	Resp.2
Si	−0.4751	−0.0823
K	−0.4634	−0.5295
Ca	0.9943	0.0906
Ti	−0.7023	−0.3806
Mn	0.2885	0.9493
Fe	−0.6268	0.1086
Rb	−0.5071	−0.2417
Sr	0.5967	−0.1424
Zr	−0.4261	−0.2747

5. Discussion

5.1. Centennial-scale monsoon variability linked to ENSO activity

The sample scores on PC1 show a long-term increasing trend, and Ti/Ca, Fe/Ca and Rb/Sr show a long-term decreasing trend (Fig. 5A, B, C, D), which indicate a decrease in rainfall during 7000–615 cal yr B.P. This pattern is consistent with other records from the ISM region (Fig. 5E-K) (e.g., Banerji et al., 2020; Berger and Loutre, 1991; Berkelhammer et al., 2012; Bird et al., 2014; Contreras-Rosales et al., 2014; Fleitmann et al., 2003; Gupta et al., 2003; Kathayat et al., 2016; Misra et al., 2019; Zhang et al., 2018). This indicates that the pattern of climate change at Lake Qionghai during this interval was dominated by the ISM, which was driven by the gradual decrease in summer insolation controlled by Earth orbital precession (Fig. 5L) (Fleitmann et al., 2003; Gupta et al., 2005; Wang et al., 2005).

Centennial-scale rainfall variations in the ISM region are highlighted in the detrended QH2019 element records (Fig. 6). During 7000–615 cal yr B.P. several centennial-scale weak monsoon intervals are evident: during ~6230–5740, ~4620–4250, ~3820–3540, ~3210–2440,

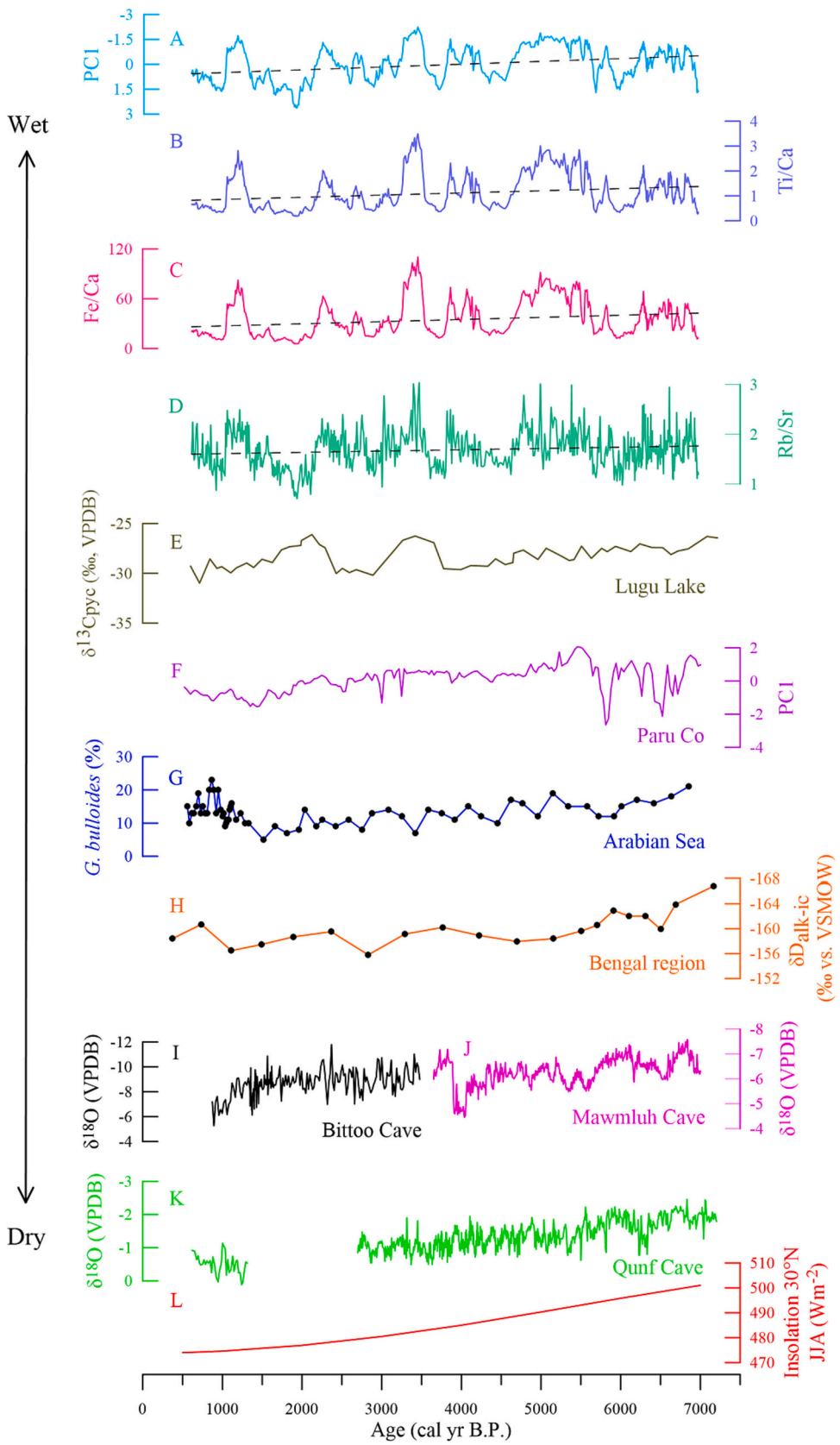

Fig. 5. Comparison of ISM records from core QH2019 from Lake Qionghai with selected paleoclimatic records from the Asian monsoon region. A) Sample scores on PC1, B) Ti/Ca, C) Fe/Ca, and D) Rb/Sr (this study). The black dashed lines are linear fits which demonstrate the general trend. E) Pyrogenic carbon record from Lake Lugu (Zhang et al., 2018). F) PC1 based on the grain size record from Paru Co (Bird et al., 2014). G) Percentages of *Globigerina bulloides* from ODP Hole 723A in the Arabian Sea (Gupta et al., 2003). H) Hydrogen isotope record (δD_{alk-ic}) from core SO188-342KL (Contreras-Rosales et al., 2014). I) Stalagmite $\delta^{18}O$ record from Bittoo Cave (Kathayat et al., 2016). J) Stalagmite $\delta^{18}O$ record from Mawmluh Cave (Berkelhammer et al., 2012). K) Stalagmite $\delta^{18}O$ record from Qunf Cave (Fleitmann et al., 2003). L) June–August averaged insolation at 30°N (Berger and Loutre, 1991). Locations of all records ate shown in Fig. 1A.

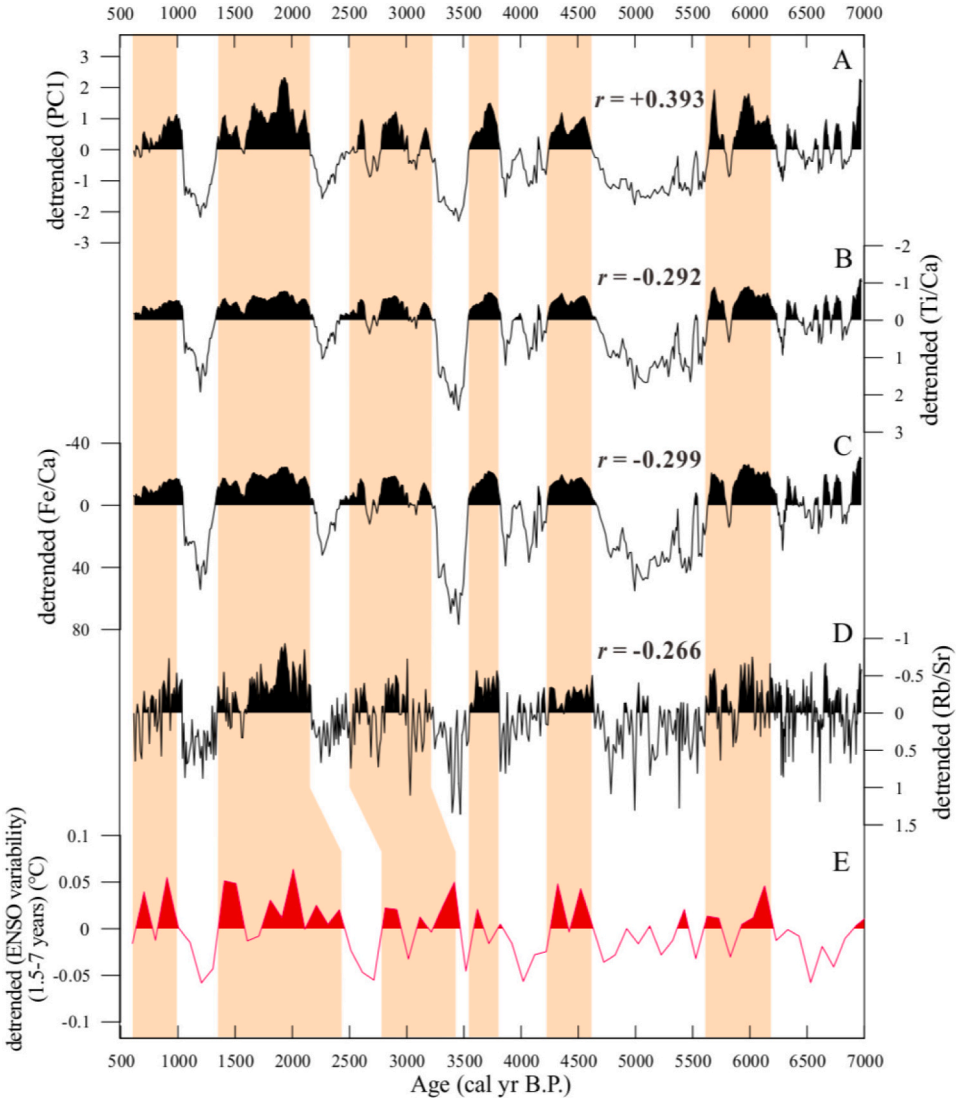

Fig. 6. Comparisons of the detrended proxy records from core QH2019 with ENSO activity during the middle to late Holocene. A) Sample scores on PC1, B) Ti/Ca, C) Fe/Ca and D) Rb/Sr record from core QH2019 (this study), and their correlation coefficients with ENSO ($p < 0.01$, $n = 6359$); E) Simulated ENSO amplitude (standard deviation of Niño 3.4 interannual (1.5–7 years) SST variability) in 100-year windows (Liu et al., 2014). Yellow bars denote dry conditions and weak monsoon intervals, corresponding to enhanced El Niño activity. Data were detrended using the detrend function in MATLAB. (For interpretation of the references to colour in this figure legend, the reader is referred to the web version of this article.)

2180–1320 and ~ 1000–615 cal yr B.P.. They are defined by PC1 values >0 and Fe/Ca, Ti/Ca and Rb/Sr values <0 (Fig. 6A, B, C, D). Most of these weak monsoon intervals are in phase with intervals of high ENSO activity (values >0), within the dating error (Fig. 6E). There is a significant negative correlation between evolution of humidity conditions at Lake Qionghai and ENSO intensity, with correlation coefficients between PC1, Fe/Ca, Ti/Ca, Rb/Sr with ENSO of 0.393, −0.292, −0.299, and − 0.266 ($p < 0.01$, $n = 6359$), respectively. These negative correlations suggest a teleconnection between ENSO-like patterns and dryness at Lake Qionghai. This confirms the observation from historical records that El Niño years are generally associated with a summer monsoon rainfall deficit in India and southwest China (Kumar et al., 1999; Ming et al., 2020; Ropelewski and Halpert, 1987).

The Lake Qionghai records clearly demonstrate the occurrence of high-frequency variations in humidity on the centennial timescale. The results of power spectrum analysis reveal statistically significant (95% significance level) periodicities centered at ~200, ~350, ~500, and ~ 800 years (Fig. 7A, B, C, D). These periodicities are consistent, within the age uncertainties, with the cycles of total solar irradiance (TSI) reconstructed from records of ^{14}C and ^{10}Be preserved within tree rings and ice cores (Hanslmeier et al., 2013; Steinhilber et al., 2012; Wanner et al., 2008). Moreover, similar periodicities have also been reported in other paleoclimatic records from the ISM region and beyond (Agnihotri et al., 2002; Dykoski et al., 2005; Neff et al., 2001; Thamban et al., 2007; Warrier et al., 2017; Zhao et al., 2010). However, the phase relationship between ISM and solar activity remains unclear. Several studies have concluded that high ISM precipitation corresponds to periods of increased solar activity (Gupta et al., 2005; Kodera, 2004; Sun et al., 2020; Xu et al., 2015), while other studies found the opposite relationship (Cui et al., 2022; Gu et al., 2020; Li et al., 2021). A nonstationary phase relationship may be related to the nonlinear response of ISM precipitation variability to solar activity (Tiwari et al., 2015; Weng, 2012), or it may be influenced by the dynamics of tropical ocean-atmosphere coupling phenomena (such as ENSO) (Berkelhammer et al., 2010; Conroy et al., 2008; Emile-Geay et al., 2007; Sun et al., 2022; Tiwari et al., 2015).

Spectral analysis of the modeled ENSO variance data reveal that it also exhibits significant centennial-scale cyclicity, centered at ~350-yr, ~500-yr and ~ 800-yr (Fig. 7E). The occurrence of similar cyclicities in the record from Lake Qionghai suggests the possible influence of ENSO variability on the study area. To further assess the relationship between the ISM record from Lake Qionghai and ENSO activity, we compared the results of PC1 and ENSO variations after band-pass filtering at 350-yr, 500-yr, and 800-yr (Fig. 8). The results indicate a highly significant positive relationship between PC1 and ENSO activity on the centennial timescale (the correlation coefficients are 0.526, 0.409 and 0.552, respectively); that is, there is a highly significant negative relationship between ISM humidity and ENSO activity. Wet/dry phases in the ISM

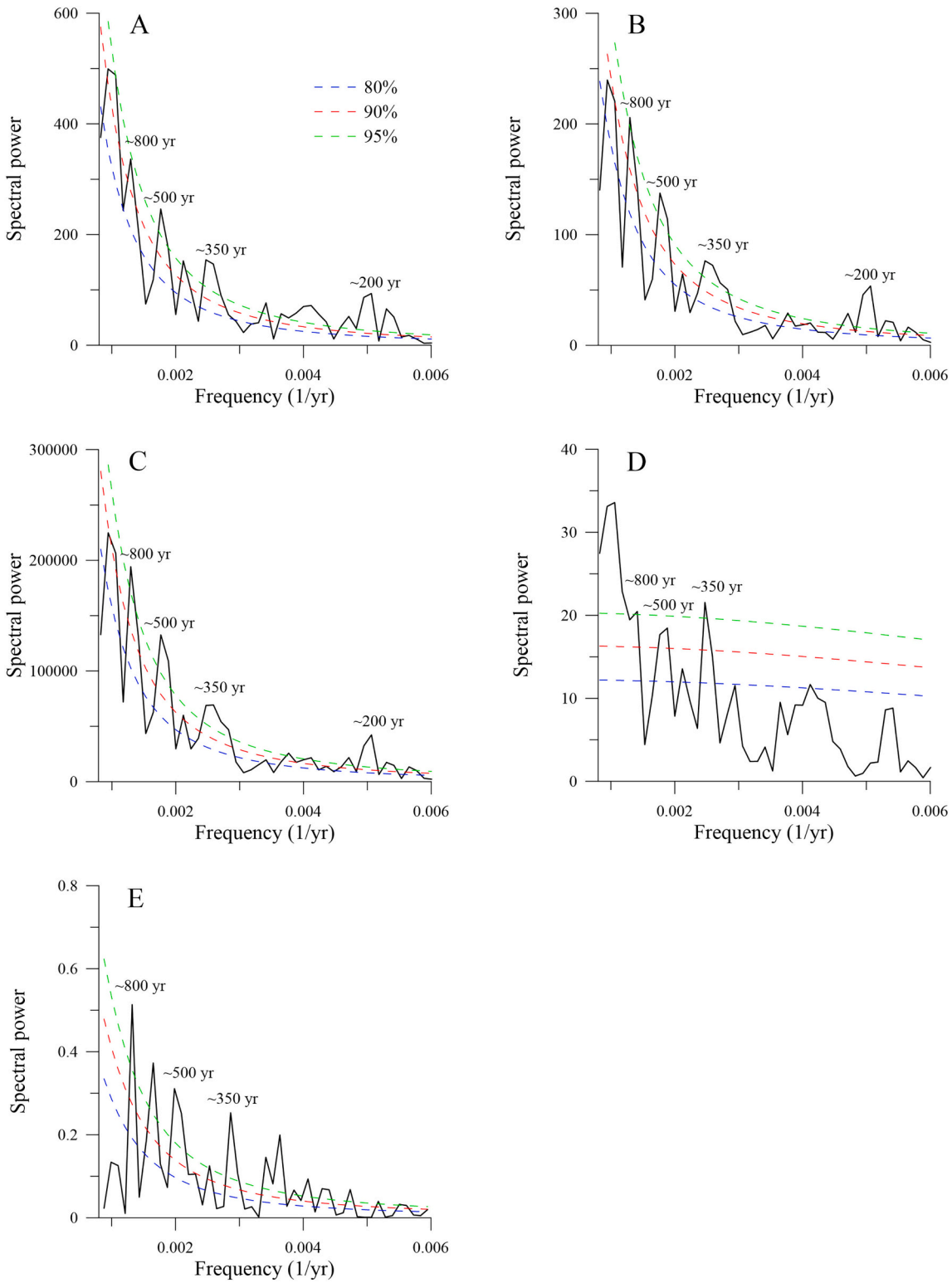

Fig. 7. Spectral analysis results for multi-proxy indicators from Lake Qionghai and ENSO activity (Liu et al., 2014). A) PC1; B) Ti/Ca; C) Fe/Ca; D) Rb/Sr; E) ENSO activity. Periodicities which exceed the 80%, 90% and 95% confidence levels (blue, red and green lines, respectively) are labeled. (For interpretation of the references to colour in this figure legend, the reader is referred to the web version of this article.)

region correspond well to weak/strong ENSO phases. However, evidently there was a delayed response of the ISM to ENSO between 3800 and 2500 cal yr B.P. in the 500-yr filter comparison, which may be due to the relatively weak influence of ENSO on the ISM at this periodicity (Fig. 8B). In addition, considering the age error, the phase relationships for the 350-yr cycle may require additional evidence for verification.

5.2. *Possible forcing mechanisms*

Numerous modern instrumental observations indicate that increased ENSO activity would increase both the average aridity and its variability

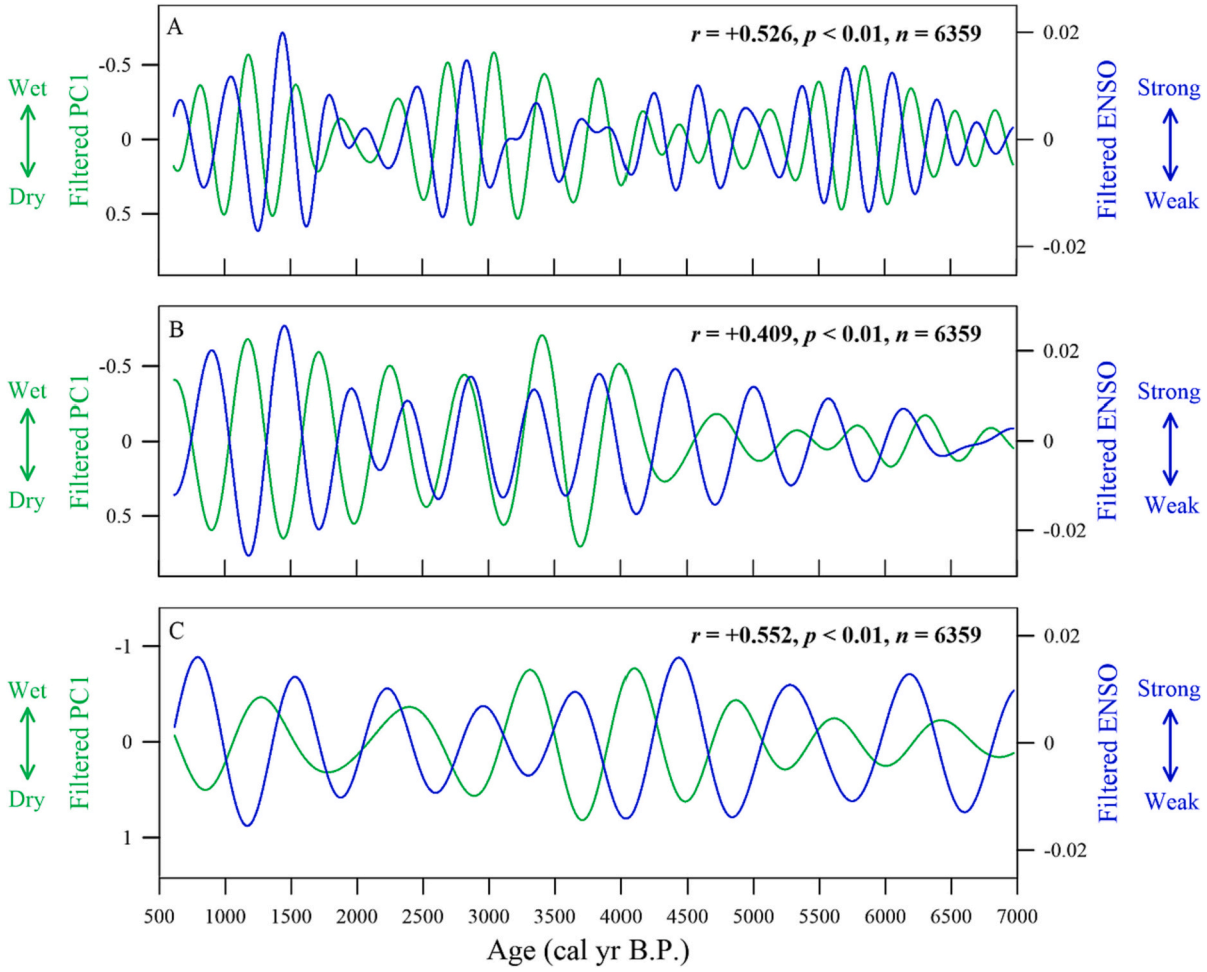

Fig. 8. Results of band-pass filtering of PC1 from Lake Qionghai (green curve) and ENSO activity (blue curve) (Liu et al., 2014). A) 350-yr band-pass filtering results; B) 500-yr band-pass filtering results; C) 800-yr band-pass filtering results. (For interpretation of the references to colour in this figure legend, the reader is referred to the web version of this article.)

in the ISM-influenced regions (Fig. 9) (Kumar et al., 2006; Shukla and Paolino, 1983; Torrence and Webster, 1999; Webster et al., 1998). ENSO originates from air-sea interactions among the sea surface temperature (SST), surface winds, and the thermocline within the tropical Pacific (Bjerknes, 1969; Jin et al., 2006; Zhang et al., 2015). The conventional interpretation of the ENSO-induced teleconnection response in the monsoon region is via large-scale east-west shifts in the tropical Walker circulation (Ropelewski and Halpert, 1987; Walker, 1918). During an El Niño event, the tropical convection and the associated rising limb of the Walker circulation normally located in the western Pacific shift towards the anomalously warm waters of the central and eastern Pacific (Cane, 2005; Fischer et al., 2005). Consequently, an anomalous atmospheric subsidence extends from the western Pacific region to the Indian subcontinent, which suppresses convection and precipitation over these regions (Ashok et al., 2004; Kumar et al., 1999; Wang et al., 2003). This coupled feedback of large-scale tropical ocean-atmosphere interactions in the equatorial Pacific region alters the rain belt and influences the ISM precipitation, and may control the occurrence of ENSO-related drought events in ISM region (Fig. 8).

Current research on the relationship between ISM and ENSO during the Holocene mostly focuses on high-resolution narrow temporal windows, or low-resolution wide temporal windows (Fig. 9). Stalagmite studies have shown that droughts occurred in southwest China under decadal El Niño-like conditions during the last 240 years, which is consistent with observational data and simulations (Tan et al., 2016). Based on phytolith and stalagmite studies over the past 1000 to 2000 years, Gu et al. (2020) and Tan et al. (2019) concluded that the occurrence of droughts during the CWP and the MWP in southwest China and the central Indo-Pacific were associated with strong El Niño conditions in the tropical Pacific. Ming et al. (2020) observed a negative correlation between sub-millennial-scale monsoon moisture variations and warm ENSO events at Lake Ruogen Co in the eastern Tibetan Plateau over the past 6000 years. The significant sub-millennial-scale dry events observed in the record from Lake Chenghai in the southeastern margin of the Qinghai-Tibet Plateau were caused by the coupling of ENSO activity and shifts in the intertropical convergence zone (Sun et al., 2017). Stalagmite $\delta^{18}O$ records from Kotumsar Cave, Central India, demonstrate that the ISM during the mid-Holocene (8.5–5.6 ka BP) was sensitive to ENSO, and inversely correlated with it (Band et al., 2018). However, a study of peats deposits in the Himalayas over the past ~8000 years suggested that the ENSO-dominated climate in the ISM region developed at ~5.5 ka BP when a reorganization of the tropical climate system ensued (Srivastava et al., 2017). Hillman et al. (2017) also suggested that the amplification of ENSO may be a potential factor for monsoon weakening since 5.0 ka BP. Other studies have indicated that the long-term influence of ENSO on the ISM began at only 2 cal ka BP (Prasad et al., 2014). For the first time our records provide evidence that the anticorrelation between ENSO and ISM on the centennial timescale occurred during the middle and late Holocene. Both previous studies and our record from Lake Qionghai (Fig. 9) indicate that ENSO modulated ISM intensity on multiple timescales during the Holocene. However, more climate records on different timescales from the ISM

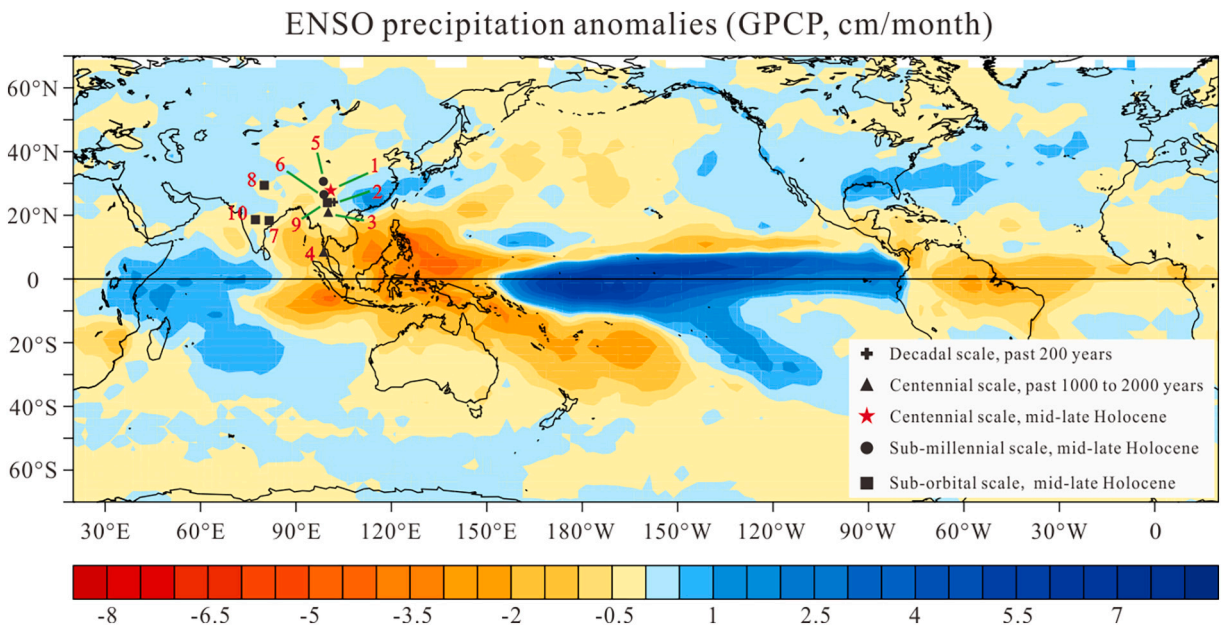

Fig. 9. Map of typical ENSO precipitation anomalies (cm/month) for all calendar months combined during the El Niño years of 1979–2006 CE (data source: http://research.jisao.washington.edu/data/gpcp/). The red star indicates the location of Lake Qionghai, and other symbols indicate the locations of other paleoclimate records which demonstrate ISM and ENSO relationships on different timescales and in different time windows, as discussed in the text: (1) Lake Qionghai (this study); (2) Xiaobailong Cave (Tan et al., 2016); (3) ML3 profile (Gu et al., 2020); (4) Klang Cave (Tan et al., 2019); (5) Lake Ruogen Co (Ming et al., 2020); (6) Lake Chenghai (Sun et al., 2017); (7) Kotumsar Cave (Band et al., 2018); (8) Kedarnath peatland (Srivastava et al., 2017); (9) Lake Xingyun (Hillman et al., 2017); (10) Lake Lonar (Prasad et al., 2014). (For interpretation of the references to colour in this figure legend, the reader is referred to the web version of this article.)

region are needed to improve our understanding of the influence of ENSO on the ISM, which could potentially improve the forecasting of future drought events in its region of influence.

6. Conclusions

We have used high-resolution XRF scanning of a sediment core from Lake Qionghai, on the southeastern Tibetan Plateau, we reconstruct changes in humidity in the ISM region from 7000 to 615 cal yr B.P. and to explore the links between the ISM and ENSO activity on the centennial timescale. Our results indicate that the climate of the ISM region during the middle and late Holocene became increasingly arid, tracking the long-term decrease in Northern Hemisphere insolation. Centennial-scale drought events were associated with the increased intensity and frequency of ENSO activity. Spectral analysis and band-pass filtering analysis show that both the inferred ISM oscillations and ENSO variability were characterized by significant 350-yr, 500-yr, and 800-yr cycles and that they exhibit a highly significant inverse relationship. Our findings emphasize that monsoon rainfall in southwest China is dominated by ENSO forcing on the centennial timescale.

CRediT authorship contribution statement

Huanyu Sun: Data curation, Formal analysis, Investigation, Methodology, Visualization, Writing – original draft. **Xingqi Liu:** Conceptualization, Formal analysis, Funding acquisition, Investigation, Project administration, Resources, Supervision, Writing – review & editing. **Xin Mao:** Investigation. **Weihan Jia:** Investigation. **Ulrike Herzschuh:** Writing – review & editing.

Declaration of Competing Interest

The authors declare that they have no known competing financial interests or personal relationships that could have appeared to influence the work reported in this paper.

Data availability

Data will be made available on request.

Acknowledgments

This work was supported by a corporative project of the National Natural Science Foundation of China (NSFC) and the German Research Foundation (DFG) (41861134030), and the National Natural Science Foundation of China (NSFC) (42272218).

Appendix A. Supplementary data

Supplementary data to this article can be found online at https://doi.org/10.1016/j.palaeo.2022.111380.

References

Adegbie, A.T., Schneider, R.R., Röhl, U., Wefer, G., 2003. Glacial millennial-scale fluctuations in central african precipitation recorded in terrigenous sediment supply and freshwater signals offshore Cameroon. Palaeogeogr. Palaeoclimatol. Palaeoecol. 197 (3–4), 323–333. https://doi.org/10.1016/s0031-0182(03)00474-7.

Agnihotri, R., Dutta, K., Bhushan, R., Somayajulu, B.L.K., 2002. Evidence for solar forcing on the indian monsoon during the last millennium. Earth Planet. Sci. Lett. 198 (3–4), 521–527. https://doi.org/10.1016/S0012-821X(02)00530-7.

Arnaud, F., Révillon, S., Debret, M., Revel, M., Chapron, E., Jacob, J., Giguet-Covex, C., Poulenard, J., Magny, M., 2012. Lake Bourget regional erosion patterns reconstruction reveals Holocene NW European Alps soil evolution and paleohydrology. Quat. Sci. Rev. 51, 81–92. https://doi.org/10.1016/j.quascirev.2012.07.025.

Ashok, K., Guan, Z., Saji, N.H., Yamagata, T., 2004. Individual and combined Influences of ENSO and the Indian Ocean Dipole on the Indian Summer Monsoon. J. Clim. 17 (16), 3141–3155. https://doi.org/10.1175/1520-0442(2004)0172.0.CO;2.

Bajard, M., Sabatier, P., David, F., Develle, A.-L., Reyss, J.-L., Fanget, B., Malet, E., Arnaud, D., Augustin, L., Crouzet, C., Poulenard, J., Arnaud, F., 2015. Erosion record in Lake La Thuile sediments (Prealps, France): evidence of montane landscape dynamics throughout the Holocene. The Holocene 26 (3), 350–364. https://doi.org/10.1177/0959683615609750.

Band, S., Yadava, M.G., Lone, M.A., Shen, C.-C., Sree, K., Ramesh, R., 2018. High-resolution mid-Holocene Indian Summer Monsoon recorded in a stalagmite from the Kotumsar Cave, Central India. Quat. Int. 479, 19–24. https://doi.org/10.1016/j.quaint.2018.01.026.

Banerji, U.S., Arulbalaji, P., Padmalal, D., 2020. Holocene climate variability and Indian Summer Monsoon: an overview. The Holocene 30 (5), 744–773. https://doi.org/10.1177/0959683619895577.
Berger, A., Loutre, M.F., 1991. Insolation values for the climate of the last 10 million years. Quat. Sci. Rev. 10, 297–317. https://doi.org/10.1016/0277-3791(91)90033-Q.
Berkelhammer, M., Sinha, A., Mudelsee, M., Cheng, H., Edwards, R.L., Cannariato, K., 2010. Persistent multidecadal power of the Indian Summer Monsoon. Earth Planet. Sci. Lett. 290 (1–2), 166–172. https://doi.org/10.1016/j.epsl.2009.12.017.
Berkelhammer, M., Sinha, A., Stott, L., Cheng, H., Pausata, F.S.R., Yoshimura, K., 2012. An abrupt Shift in the Indian Monsoon 4000 years Ago. Geophys. Monogr. Ser. 198, 75–88. https://doi.org/10.1029/2012GM001207.
Bird, B.W., Polisar, P.J., Lei, Y., Thompson, L.G., Yao, T., Finney, B.P., Bain, D.J., Pompeani, D.P., Steinman, B.A., 2014. A Tibetan lake sediment record of Holocene indian summer monsoon variability. Earth Planet. Sci. Lett. 399, 92–102. https://doi.org/10.1016/j.epsl.2014.05.017.
Bjerknes, J., 1969. Atmospheric teleconnections from the equatorial Pacific. Mon. Weather Rev. 97 (3), 163–172. https://doi.org/10.1175/1520-0493(1969)0972.3.CO;2.
Blaauw, M., Christen, J.A., 2011. Flexible paleoclimate age-depth models using an autoregressive gamma process. Bayesian Anal. 6 (3), 457–474. https://doi.org/10.1214/11-ba618.
Cai, Y., Fung, I.Y., Edwards, R.L., An, Z., Cheng, H., Lee, J.-E., Tan, L., Shen, C.-C., Wang, X., Day, J.A., Zhou, W., Kelly, M.J., Chiang, J.C.H., 2015. Variability of stalagmite-inferred indian monsoon precipitation over the past 252,000 y. Proc. Natl. Acad. Sci. 112 (10), 2954–2959. https://doi.org/10.1073/pnas.1424035112.
Cane, M.A., 2005. The evolution of El Niño, past and future. Earth Planet. Sci. Lett. 230 (3–4), 227–240. https://doi.org/10.1016/j.epsl.2004.12.003.
Chen, N., Chen, M., Li, J., He, N., Deng, M., Iqbal Tanoli, J., Cai, M., 2015. Effects of human activity on erosion, sedimentation and debris flow activity – A case study of the Qionghai Lake watershed, southeastern Tibetan Plateau, China. The Holocene 25 (6), 973–988. https://doi.org/10.1177/0959683615574893.
Clemens, S.C., Prell, W.L., 2003. A 350,000 year summer-monsoon multi-proxy stack from the Owen Ridge, Northern Arabian Sea. Marine Geol. 201 (1–3), 35–51. https://doi.org/10.1016/s0025-3227(03)00207-x.
Clift, P.D., Wan, S., Blusztajn, J., 2014. Reconstructing chemical weathering, physical erosion and monsoon intensity since 25 Ma in the northern South China Sea: a review of competing proxies. Earth Sci. Rev. 130, 86–102. https://doi.org/10.1016/j.earscirev.2014.01.002.
Conroy, J.L., Overpeck, J.T., Cole, J.E., Shanahan, T.M., Steinitz-Kannan, M., 2008. Holocene changes in eastern tropical Pacific climate inferred from a Galápagos lake sediment record. Quat. Sci. Rev. 27 (11–12), 1166–1180. https://doi.org/10.1016/j.quascirev.2008.02.015.
Contreras-Rosales, L.A., Jennerjahn, T., Tharammal, T., Meyer, V., Lückge, A., Paul, A., Schefuß, E., 2014. Evolution of the Indian Summer Monsoon and terrestrial vegetation in the Bengal region during the past 18 ka. Quat. Sci. Rev. 102, 133–148. https://doi.org/10.1016/j.quascirev.2014.08.010.
Croudace, I.W., Rindby, A., Rothwell, R.G., 2006. ITRAX: description and evaluation of a new multi-function X-ray core scanner. Geol. Soc. Lond. Spec. Publ. 267 (1), 51–63. https://doi.org/10.1144/GSL.SP.2006.267.01.04.
Cui, Y., Zhao, K., Shao, X., Chen, S., Wang, Y., 2022. Mechanism of asian monsoon precipitation variation and solar activity on a century time scale over the past 1000 years. Carsol. Sin. 41 (1), 143–152. https://doi.org/10.11932/karst20220108 (in Chinese with English abstract).
Deser, C., Alexander, M.A., Xie, S.P., Phillips, A.S., 2010. Sea surface temperature variability: patterns and mechanisms. Annu. Rev.Marine Sci. 2, 115–143. https://doi.org/10.1146/annurev-marine-120408-151453.
Dykoski, C.A., Edwards, R.L., Cheng, H., Yuan, D., Cai, Y., Zhang, M., Lin, Y., Qing, J., An, Z., Revenaugh, J., 2005. A high-resolution, absolute-dated Holocene and deglacial Asian monsoon record from Dongge Cave, China. Earth and Planetary Science Letters 233 (1–2), 71–86. https://doi.org/10.1016/j.epsl.2005.01.036.
Emile-Geay, J., Cane, M., Seager, R., Kaplan, A., Almasi, P., 2007. El Niño as a mediator of the solar influence on climate. Paleoceanography 22 (3), 1–16. https://doi.org/10.1029/2006pa001304.
Fernández, M., Björck, S., Wohlfarth, B., Maidana, N.I., Unkel, I., Van der Putten, N., 2013. Diatom assemblage changes in lacustrine sediments from Isla de los Estados, southernmost South America, in response to shifts in the southwesterly wind belt during the last deglaciation. J. Paleolimnol. 50 (4), 433–446. https://doi.org/10.1007/s10933-013-9736-4.
Fischer, A.S., Terray, P., Guilyardi, E., Gualdi, S., Delecluse, P., 2005. Two independent triggers for the Indian Ocean Dipole/Zonal Mode in a coupled GCM. J. Clim. 18, 3428–3449. https://doi.org/10.1175/JCLI3478.1.
Fleitmann, D., Burns, S.J., Mudelsee, M., Neff, U., Kramers, J., Mangini, A., Matter, A., 2003. Holocene forcing of the indian monsoon recorded in a stalagmite from southern Oman. Science 300 (5626), 1737–1739. https://doi.org/10.1126/science.1083130.
Fleitmann, D., Burns, S.J., Mangini, A., Mudelsee, M., Kramers, J., Villa, I., Neff, U., Al-Subbary, A.A., Buettner, A., Hippler, D., Matter, A., 2007. Holocene ITCZ and indian monsoon dynamics recorded in stalagmites from Oman and Yemen (Socotra). Quat. Sci. Rev. 26, 170–188. https://doi.org/10.1016/j.quascirev.2006.04.012.
Gu, Y., Liu, H., Traoré, D.D., Huang, C., 2020. ENSO-related droughts and ISM variations during the last millennium in tropical Southwest China. Clim. Dyn. 54 (1–2), 649–659. https://doi.org/10.1007/s00382-019-05019-1.
Guo, Q., Li, Y., Huang, Q., Wang, L., Ye, S., 2014. Historical Seismic Landslide of Zemu River Fault Zone. J. Catastrophol. 29 (2), 182–187. https://doi.org/10.3969/j.issn.1000-811X.2014.02.034 (in Chinese with English abstract).
Gupta, A.K., Anderson, D.M., Overpeck, J.T., 2003. Abrupt changes in the asian southwest monsoon during the Holocene and their links to the North Atlantic Ocean. Nature 421 (6921), 354–357. https://doi.org/10.1038/nature01340.
Gupta, A.K., Das, M., Anderson, D.M., 2005. Solar influence on the indian summer monsoon during the Holocene. Geophys. Res. Lett. 32 (17) https://doi.org/10.1029/2005gl022685.
Hammer, O., Harper, D.A.T., Ryan, P.D., 2001. Past: Paleontological Statistics Software Package for Education and Data Analysis. Palaeontol. Electron. 4 (1), 1–9. https://palaeo-electronica.org/2001_1/past/issue1_01.htm.
Hanslmeier, A., Brajša, R., Čalogović, J., Vršnak, B., Ruždjak, D., Steinhilber, F., MacLeod, C.L., Ivezić, Ž., Skokić, I., 2013. The chaotic solar cycle. Astron. Astrophys. 550, A6. https://doi.org/10.1051/0004-6361/201015215.
Haug, G.H., Gunther, D., Peterson, L.C., Sigman, D.M., Hughen, K.A., Aeschlimann, B., 2003. Climate and the collapse of Maya civilization. Science 299 (5613), 1731–1735. https://doi.org/10.1126/science.1080444.
Haug, G.H., Hughen, K.A., Sigman, D.M., Peterson, L.C., Rohl, U., 2001. Southward migration of the intertropical convergence zone through the Holocene. Science 293, 1304–1308. https://doi.org/10.1126/science.1059725.
Hillman, A.L., Abbott, M.B., Finkenbinder, M.S., Yu, J., 2017. An 8,600 year lacustrine record of summer monsoon variability from Yunnan, China. Quat. Sci. Rev. 174, 120–132. https://doi.org/10.1016/j.quascirev.2017.09.005.
Hong, Y.T., Hong, B., Lin, Q.H., Shibata, Y., Hirota, M., Zhu, Y.X., Leng, X.T., Wang, Y., Wang, H., Yi, L., 2005. Inverse phase oscillations between the East asian and Indian Ocean summer monsoons during the last 12000 years and paleo-El Niño. Earth Planet. Sci. Lett. 231 (3–4), 337–346. https://doi.org/10.1016/j.epsl.2004.12.025.
Jin, F.-F., Kim, S.T., Bejarano, L., 2006. A coupled-stability index for ENSO. Geophys. Res. Lett. 33 (23) https://doi.org/10.1029/2006gl027221.
Kasper, T., Haberzettl, T., Doberschütz, S., Daut, G., Wang, J., Zhu, L., Nowaczyk, N., Mäusbacher, R., 2012. Indian Ocean Summer Monsoon (IOSM)-dynamics within the past 4 ka recorded in the sediments of Lake Nam Co, central Tibetan Plateau (China). Quat. Sci. Rev. 39, 73–85. https://doi.org/10.1016/j.quascirev.2012.02.011.
Kasper, T., Haberzettl, T., Wang, J., Daut, G., DoberschÜtz, S., Zhu, L., Mausbacher, R., 2015. Hydrological variations on the Central Tibetan Plateau since the Last Glacial Maximum and their teleconnection to inter-regional and hemispheric climate variations. J. Quat. Sci. 30 (1), 70–78. https://doi.org/10.1002/jqs.2759.
Kathayat, G., Cheng, H., Sinha, A., Spotl, C., Edwards, R.L., Zhang, H., Li, X., Yi, L., Ning, Y., Cai, Y., Lui, W.L., Breitenbach, S.F., 2016. Indian monsoon variability on millennial-orbital timescales. Sci. Rep. 6, 24374. https://doi.org/10.1038/srep24374.
Kodera, K., 2004. Solar influence on the Indian Ocean Monsoon through dynamical processes. Geophys. Res. Lett. 31 (24) https://doi.org/10.1029/2004gl020928.
Koinig, K.A., Shotyk, W., Lotter, A.F., Ohlendorf, C., Sturm, M., 2003. 9000 years of geochemical evolution of lithogenic major and trace elements in the sediment of an alpine lake: the role of climate, vegetation, and land-use history. J. Paleolimnol. 30, 307–320. https://doi.org/10.1023/A:1026080712312.
Kumar, K.K., Rajagopalan, B., Cane, M.A., 1999. On the weakening Relationship between the lndian Monsoon and ENSO. Nature 284 (5423), 2156–2159. https://doi.org/10.1126/science.284.5423.2156.
Kumar, K.K., Rajagopalan, B., Hoerling, M., Bates, G., Cane, M., 2006. Unraveling the mystery of indian monsoon failure during El Niño. Science 314 (5796), 115–119. https://doi.org/10.1126/science.1131152.
Kutzbach, J.E., Liu, X., Liu, Z., Chen, G., 2008. Simulation of the evolutionary response of global summer monsoons to orbital forcing over the past 280,000 years. Clim. Dyn. 30 (6), 567–579. https://doi.org/10.1007/s00382-007-0308-z.
Kylander, M.E., Ampel, L., Wohlfarth, B., Veres, D., 2011. High-resolution X-ray fluorescence core scanning analysis of Les Echets (France) sedimentary sequence: new insights from chemical proxies. J. Quat. Sci. 26 (1), 109–117. https://doi.org/10.1002/jqs.1438.
Leuschner, D.C., Sirocko, F., 2003. Orbital insolation forcing of the Indian Monsoon – a motor for global climate changes? Palaeogeogr. Palaeoclimatol. Palaeoecol. 197 (1–2), 83–95. https://doi.org/10.1016/s0031-0182(03)00387-0.
Li, H., Xu, D., Shen, C., Cui, A., Zuo, X., Dong, Y., Wang, C., Jin, Y., Yu, Y., Wu, N., Lu, H., 2021. Multi-centennial climate cycles and their impact on the Tubo Dynasty in the southern Tibetan Plateau. Palaeogeogr. Palaeoclimatol. Palaeoecol. 578, 110584 https://doi.org/10.1016/j.palaeo.2021.110584.
Li, K., Liu, X., Wang, Y., Herzschuh, U., Ni, J., Liao, M., Xiao, X., 2017. Late Holocene vegetation and climate change on the southeastern Tibetan Plateau: Implications for the Indian Summer Monsoon and links to the Indian Ocean Dipole. Quat. Sci. Rev. 177, 235–245. https://doi.org/10.1016/j.quascirev.2017.10.020.
Li, M., Hinnov, L.A., Kump, L.R., 2019. Acycle: Time-series analysis software for paleoclimate research and education. Comput. Geosci. 127, 12–22. https://doi.org/10.1016/j.cageo.2019.02.011.
Li, X., Liang, J., Hou, J., Zhang, W., 2015. Centennial-scale climate variability during the past 2000 years on the central Tibetan Plateau. The Holocene 25 (6), 892–899. https://doi.org/10.1177/0959683615572852.
Liu, G., Li, X., Chiang, H.-W., Cheng, H., Yuan, S., Chawchai, S., He, S., Lu, Y., Aung, L.T., Maung, P.M., Tun, W.N., Oo, K.M., Wang, X., 2020. On the glacial-interglacial variability of the Asian monsoon in speleothem δ18O records. Sci. Adv. 6 (7), eaay8189 https://doi.org/10.1126/sciadv.aay8189.
Liu, Z., Lu, Z., Wen, X., Otto-Bliesner, B.L., Timmermann, A., Cobb, K.M., 2014. Evolution and forcing mechanisms of El Nino over the past 21,000 years. Nature 515 (7528), 550–553. https://doi.org/10.1038/nature13963.
Marshall, M.H., Lamb, H.F., Huws, D., Davies, S.J., Bates, R., Bloemendal, J., Boyle, J., Leng, M.J., Umer, M., Bryant, C., 2011. Late Pleistocene and Holocene drought events at Lake Tana, the source of the Blue Nile. Glob. Planet. Chang. 78 (3–4), 147–161. https://doi.org/10.1016/j.gloplacha.2011.06.004.

McPhaden, M.J., Zebiak, S.E., Glantz, M.H., 2006. ENSO as an integrating concept in earth science. Science 314 (5806), 1740–1745. https://doi.org/10.1126/science.1132588.

Ming, G., Zhou, W., Cheng, P., Wang, H., Xian, F., Fu, Y., Wu, S., Du, H., 2020. Lacustrine record from the eastern Tibetan Plateau associated with asian summer monsoon changes over the past ~ 6 ka and its links with solar and ENSO activity. Clim. Dyn. 55 (5–6), 1075–1086. https://doi.org/10.1007/s00382-020-05312-4.

Misra, P., Tandon, S.K., Sinha, R., 2019. Holocene climate records from lake sediments in India: Assessment of coherence across climate zones. Earth Sci. Rev. 190, 370–397. https://doi.org/10.1016/j.earscirev.2018.12.017.

Morellón, M., Valero-Garcés, B., Vegas-Vilarrúbia, T., González-Sampériz, P., Romero, Ó., Delgado-Huertas, A., Mata, P., Moreno, A., Rico, M., Corella, J.P., 2009. Lateglacial and Holocene palaeohydrology in the western Mediterranean region: the Lake Estanya record (NE Spain). Quat. Sci. Rev. 28 (25–26), 2582–2599. https://doi.org/10.1016/j.quascirev.2009.05.014.

Neff, U., Burns, S.J., Mangini, A., Fleitmann, D., Matter, A., 2001. Strong coherence between solar variability and the monsoon in Oman between 9 and 6 kyr ago. Nature 411 (6835), 290–293. https://doi.org/10.1038/35077048.

Overpeck, J., Anderson, D., Trumbore, S., Prell, W., 1996. The southwest Indian Monsoon over the last 18 000 years. Clim. Dyn. 12 (3), 213–225. https://doi.org/10.1007/BF00211619.

Prasad, S., Anoop, A., Riedel, N., Sarkar, S., Menzel, P., Basavaiah, N., Krishnan, R., Fuller, D., Plessen, B., Gaye, B., Röhl, U., Wilkes, H., Sachse, D., Sawant, R., Wiesner, M.G., Stebich, M., 2014. Prolonged monsoon droughts and links to Indo-Pacific warm pool: a Holocene record from Lonar Lake, Central India. Earth Planet. Sci. Lett. 391, 171–182. https://doi.org/10.1016/j.epsl.2014.01.043.

Reason, C.J.C., Allan, R.J., Lindesay, J.A., Ansell, T.J., 2000. ENSO and climatic signals across the Indian Ocean Basin in the global context: part I, interannual composite patterns. Int. J. Climatol. 20 (11), 1285–1327.

Reimer, P.J., Austin, W.E.N., Bard, E., Bayliss, A., Blackwell, P.G., Bronk Ramsey, C., Butzin, M., Cheng, H., Edwards, R.L., Friedrich, M., Grootes, P.M., Guilderson, T.P., Hajdas, I., Heaton, T.J., Hogg, A.G., Hughen, K.A., Kromer, B., Manning, S.W., Muscheler, R., Palmer, J.G., Pearson, C., van der Plicht, J., Reimer, R.W., Richards, D.A., Scott, E.M., Southon, J.R., Turney, C.S.M., Wacker, L., Adolphi, F., Büntgen, U., Capano, M., Fahrni, S.M., Fogtmann-Schulz, A., Friedrich, R., Köhler, P., Kudsk, S., Miyake, F., Olsen, J., Reinig, F., Sakamoto, M., Sookdeo, A., Talamo, S., 2020. The IntCal20 Northern Hemisphere Radiocarbon Age Calibration Curve (0–55 cal kBP). Radiocarbon 62 (4), 725–757. https://doi.org/10.1017/rdc.2020.41.

Ropelewski, C.F., Halpert, M.S., 1987. Global and Regional Scale Precipitation patterns Associated with the El Ni??o/Southern Oscillation. Mon. Weather Rev. 115 (8), 1606–1626. https://doi.org/10.1175/1520-0493(1987)1152.0.CO;2.

Shukla, J., Paolino, D.A., 1983. The southern oscillation and long-range forecasting of the summer monsoon rainfall over India. Mon. Weather Rev. 111 (9), 1830–1837. https://doi.org/10.1175/1520-0493(1983)1112.0.CO;2.

Srivastava, P., Agnihotri, R., Sharma, D., Meena, N., Sundriyal, Y.P., Saxena, A., Bhushan, R., Sawlani, R., Banerji, U.S., Sharma, C., Bisht, P., Rana, N., Jayangondaperumal, R., 2017. 8000-year monsoonal record from Himalaya revealing reinforcement of tropical and global climate systems since mid-Holocene. Sci. Rep. 7 (1), 14515. https://doi.org/10.1038/s41598-017-15143-9.

Steinhilber, F., Abreu, J.A., Beer, J., Brunner, I., Christl, M., Fischer, H., Heikkila, U., Kubik, P.W., Mann, M., McCracken, K.G., Miller, H., Miyahara, H., Oerter, H., Wilhelms, F., 2012. 9,400 years of cosmic radiation and solar activity from ice cores and tree rings. Proc. Natl. Acad. Sci. U. S. A. 109 (16), 5967–5971. https://doi.org/10.1073/pnas.1118965109.

Stuut, J.-B.W., Temmesfeld, F., De Deckker, P., 2014. A 550 ka record of aeolian activity near North West Cape, Australia: inferences from grain-size distributions and bulk chemistry of SE Indian Ocean deep-sea sediments. Quat. Sci. Rev. 83, 83–94. https://doi.org/10.1016/j.quascirev.2013.11.003.

Sun, W., Zhang, E., Liu, E., Ji, M., Chen, R., Zhao, C., Shen, J., Li, Y., 2017. Oscillations in the indian summer monsoon during the Holocene inferred from a stable isotope record from pyrogenic carbon from Lake Chenghai, Southwest China. J. Asian Earth Sci. 134, 29–36. https://doi.org/10.1016/j.jseaes.2016.11.002.

Sun, W., Liu, J., Wang, B., Chen, D., Wan, L., Wang, J., 2022. Holocene Multi-Centennial Variations of the Asian Summer Monsoon Triggered by Solar activity. Geophys. Res. Lett. 49 (13) https://doi.org/10.1029/2022gl098625.

Sun, Z., Yuan, K., Hou, X., Ji, K., Li, C.-G., Wang, M., Hou, J., 2020. Centennial-scale interplay between the Indian Summer Monsoon and the Westerlies revealed from Ngamring Co, southern Tibetan Plateau. The Holocene 30 (8), 1163–1173. https://doi.org/10.1177/0959683620913930.

Tan, L., Cai, Y., An, Z., Cheng, H., Shen, C.-C., Gao, Y., Edwards, R.L., 2016. Decreasing monsoon precipitation in Southwest China during the last 240 years associated with the warming of tropical ocean. Clim. Dyn. 48 (5–6), 1769–1778. https://doi.org/10.1007/s00382-016-3171-y.

Tan, L., Shen, C.C., Lowemark, L., Chawchai, S., Edwards, R.L., Cai, Y., Breitenbach, S.F. M., Cheng, H., Chou, Y.C., Duerrast, H., Partin, J.W., Cai, W., Chabangborn, A., Gao, Y., Kwiecien, O., Wu, C.C., Shi, Z., Hsu, H.H., Wohlfarth, B., 2019. Rainfall variations in central Indo-Pacific over the past 2,700 y. Proc. Natl. Acad. Sci. 116 (35), 17201–17206. https://doi.org/10.1073/pnas.1903167116.

Tejavath, C.T., Ashok, K., Chakraborty, S., Ramesh, R., 2019. A PMIP3 narrative of modulation of ENSO teleconnections to the indian summer monsoon by background changes in the last Millennium. Clim. Dyn. 53 (5–6), 3445–3461. https://doi.org/10.1007/s00382-019-04718-z.

ter Braak, C.J.F., Smilauer, P., 2012. Canoco reference manual and user's guide: software for ordination, version 5.0.

Thamban, M., Kawahata, H., Rao, V.P., 2007. Indian summer monsoon variability during the holocene as recorded in sediments of the Arabian Sea: timing and implications. J. Oceanogr. 63 (6), 1009–1020. https://doi.org/10.1007/s10872-007-0084-8.

Tiwari, M., Nagoji, S.S., Ganeshram, R.S., 2015. Multi-centennial scale SST and indian summer monsoon precipitation variability since the mid-Holocene and its nonlinear response to solar activity. The Holocene 25 (9), 1415–1424. https://doi.org/10.1177/0959683615585840.

Torrence, C., Webster, P.J., 1999. Interdecadal changes in the ENSO–monsoon system. J. Clim. 12 (8), 2679–2690. https://doi.org/10.1175/1520-0442(1999)0122.0.CO;2.

Walker, G.T., 1918. Correlation in seasonal variations of weather. Q. J. R. Meteorol. Soc. 44, 223–234.

Wang, B., Clemens, S.C., Liu, P., 2003. Contrasting the indian and East asian monsoons: implications on geologic timescales. Mar. Geol. 201 (1–3), 5–21. https://doi.org/10.1016/s0025-3227(03)00196-8.

Wang, B., Yang, J., Zhou, T., Wang, B., 2008. Interdecadal changes in the Major Modes of Asian-Australian Monsoon Variability: Strengthening Relationship with ENSO since the late 1970s*. J. Clim. 21 (8), 1771–1789. https://doi.org/10.1175/2007jcli1981.1.

Wang, Y.J., Cheng, H., Edwards, R.L., He, Y.Q., Kong, X.G., An, Z.S., Wu, J., Kelly, M.J., Dykoski, C.A., Li, X., 2005. The Holocene Asian Monsoon: Links to Solar changes and North Atlantic climate. Science 308 (5723), 854–857. https://doi.org/10.1126/science.1106296.

Wanner, H., Beer, J., Bütikofer, J., Crowley, T.J., Cubasch, U., Flückiger, J., Goosse, H., Grosjean, M., Joos, F., Kaplan, J.O., Küttel, M., Müller, S.A., Prentice, I.C., Solomina, O., Stocker, T.F., Tarasov, P., Wagner, M., Widmann, M., 2008. Mid- to late Holocene climate change: an overview. Quat. Sci. Rev. 27 (19–20), 1791–1828. https://doi.org/10.1016/j.quascirev.2008.06.013.

Warrier, A.K., Sandeep, K., Shankar, R., 2017. Climatic periodicities recorded in lake sediment magnetic susceptibility data: further evidence for solar forcing on indian summer monsoon. Geosci. Front. 8, 1349–1355. https://doi.org/10.1016/j.gsf.2017.01.004.

Webster, P.J., Magaña, V.O., Palmer, T.N., Shukla, J., Tomas, R.A., Yanai, M., Yasunari, T., 1998. Monsoons: Processes, predictability, and the prospects for prediction. J. Geophys. Res. Oceans 103 (C7), 14451–14510. https://doi.org/10.1029/97jc02719.

Weltje, G.J., Bloemsma, M.R., Tjallingii, R., Heslop, D., Röhl, U., Croudace, I.W., 2015. In: Croudace, I.W., Rothwell, R.G. (Eds.), Prediction of Geochemical Composition from XRF Core Scanner Data: A New Multivariate Approach Including Automatic Selection of Calibration Samples and Quantification of Uncertainties, Micro-XRF Studies of Sediment Cores, 17. Springer Netherlands, Dordrecht, pp. 507–534. https://doi.org/10.1007/978-94-017-9849-5_21.

Weng, H., 2012. Impacts of multi-scale solar activity on climate. Part II: Dominant timescales in decadal-centennial climate variability. Adv. Atmos. Sci. 29 (4), 887–908. https://doi.org/10.1007/s00376-012-1239-0.

Xu, H., Yeager, K.M., Lan, J., Liu, B., Sheng, E., Zhou, X., 2015. Abrupt Holocene Indian Summer Monsoon failures: a primary response to solar activity? The Holocene 25 (4), 677–685. https://doi.org/10.1177/0959683614566252.

Yuan, D., Cheng, H., Edwards, R.L., Dykoski, C.A., Kelly, M.J., Zhang, M., Qing, J., Lin, Y., Wang, Y., Wu, J., Dorale, J.A., An, Z., Cai, Y., 2004. Timing, duration, and transitions of the last interglacial asian monsoon. Science 304 (5670), 575–578. https://doi.org/10.1126/science.1091220.

Zhang, E., Sun, W., Chang, J., Ning, D., Shulmeister, J., 2018. Variations of the indian summer monsoon over the last 30 000 years inferred from a pyrogenic carbon record from south-West China. J. Quat. Sci. 33 (1), 131–138. https://doi.org/10.1002/jqs.3008.

Zhang, E., Zhao, C., Xue, B., Liu, Z., Yu, Z., Chen, R., Shen, J., 2017. Millennial-scale hydroclimate variations in Southwest China linked to tropical Indian Ocean since the last Glacial Maximum. Geology 45 (5), 435–438. https://doi.org/10.1130/g38309.1.

Zhang, R.H., Gao, C., Kang, X., Zhi, H., Wang, Z., Feng, L., 2015. ENSO Modulations due to Interannual Variability of Freshwater Forcing and Ocean Biology-induced heating in the Tropical Pacific. Sci. Rep. 5, 18506. https://doi.org/10.1038/srep18506.

Zhao, C., Yu, Z., Ito, E., Zhao, Y., 2010. Holocene climate trend, variability, and shift documented by lacustrine stable-isotope record in the northeastern United States. Quat. Sci. Rev. 29 (15–16), 1831–1843. https://doi.org/10.1016/j.quascirev.2010.03.018.

Zhu, S., 2005. Studies on the Yis Ethnic Historical Geography: Economic Development and Environmental Changes of Sichuan Yis Ethnic Districts in History. Sichuan University, Chengdu.

Zhu, S., 2011. Exploitation history of Main Forest Resources in Liangshan Yi Nationality Area, Sichuan Province. J. Beijing Forest. Univ. (Soc. Sci.) 101, 31–38. https://doi.org/10.13931/j.cnki.bjfuss.2011.01.008 (in Chinese with English abstract).